# Angewandte Chemie

## Akzeptierter Artikel

**Titel:** High-Energy Aqueous Magnesium Hybrid Full Batteries Enabled by Carrier-Hosting Potential Compensation

**Autoren:** Yongchao Tang, Xuejin Li, Haiming Lv, Wenlong Wang, Qi Yang, Chunyi Zhi, and Hongfei Li

WILEY-VCH

# High-Energy Aqueous Magnesium Hybrid Full Batteries Enabled by Carrier-Hosting Potential Compensation

Yongchao Tang,[a,b] [1] Xuejin Li,[a,b] [1] Haiming Lv,[a,b] Wenlong Wang,[a,b] Qi Yang,[c] Chunyi Zhi,*[a,c]

Hongfei Li*[a]

[a]   Dr. Y. Tang, Dr. X. Li, Dr. H. Lv, Prof. W. Wang, Prof. H. Li, Prof. C. Zhi
      Songshan Lake Materials Laboratory
      Dongguan, Guangdong, 523808 China
      E-mail: cy.zhi@cityu.edu.hk; lihf@sslab.org.cn
[b]   Dr. Y. Tang, Dr. X. Li, Dr. H. Lv, Prof. W. Wang
      Beijing Key Laboratory for New Energy Materials and Devices
      Beijing National Laboratory for Condensed Matter Physics, Institute of Physics, CAS, Beijing, 100190 China
[c]   Dr. Q. Yang, Prof. C. Zhi
      Department of Materials Science and Engineering
      City University of Hong Kong, 83 Tat Chee Avenue, Hong Kong, China
[1]   These authors contributed equally to this work.

      Supporting information for this article is given via a link at the end of the document.

**Abstract:** Underachieved capacity and low voltage plateau is ubiquitous in conventional aqueous magnesium ion full batteries. Such limitations originate from insufficient electrochemistry and low carrier-hosting ((de)intercalation) potential of electrode materials. Herein, via a strategy of enhancing the electrochemistry with carrier-hosting potential compensation, high-energy $Mg^{2+}/Na^+$ hybrid batteries are achieved. Typically, an unprecedented $Mg_{1.5}VCr(PO_4)_3$ (MVCP) cathode is coupled with $FeVO_4$ (FVO) anode in a new aqueous/organic hybrid electrolyte, realizing a reliable high-voltage operation. This operation enables more sufficient (de)intercalation of hybrid carriers ($Mg^{2+}/Na^+$), thereby enhancing the reversible capacity remarkably (233.4 mA h $g^{-1}$ at 0.5 A $g^{-1}$, 92.7 Wh $kg^{-1}_{electrode}$, i.e. ≥1.75-fold higher than those in conventional aqueous electrolytes). Simultaneously, resorting to the relatively high $Na^+$-hosting potential in electrodes, the low $Mg^{2+}$-hosting potential flaw is well-compensated. This synergistically widens/elevates the discharge plateau of the full battery up to 1.50 V. After 1350 cycles at 1 A $g^{-1}$, a low capacity decay of 0.018% per cycle is obtained, and the plateau is well retained. Mechanism study further reveals an unusual phase transformation of FVO to $Fe_2V_3$ and the low-lattice-strain pseudocapacitive (de)intercalation chemistry of MVCP. The
proposed strategy would promote the exploration of other high-energy aqueous hybrid batteries.

## Introduction

Earth-abundant magnesium resource makes aqueous magnesium-ion batteries be endowed with high expectations to synchronously address safety and cost issues.[1] These batteries typically consist of (de)intercalated-type cathodes (e.g. manganese oxides or $Li_3V_2(PO_4)_3$) and anodes (e.g. $FeVO_4$ or vanadium oxides), and are usually operated in aqueous electrolytes with operation voltages below 2 V.[2] Limited by insufficient (de)intercalation chemistry allowed by conventional aqueous electrolytes and the intrinsic low hosting (i.e. (de)intercalation) potential of electrode materials, current aqueous magnesium-ion batteries still face intractable challenges including low voltage plateaus (<1.00 V) and low capacities (70–100 mA h $g^{-1}$).[3] A pivotal solution is based on the use of advanced host materials to unveil the exotic electrochemical behaviors of batteries, especially at a high operation voltage.[4]
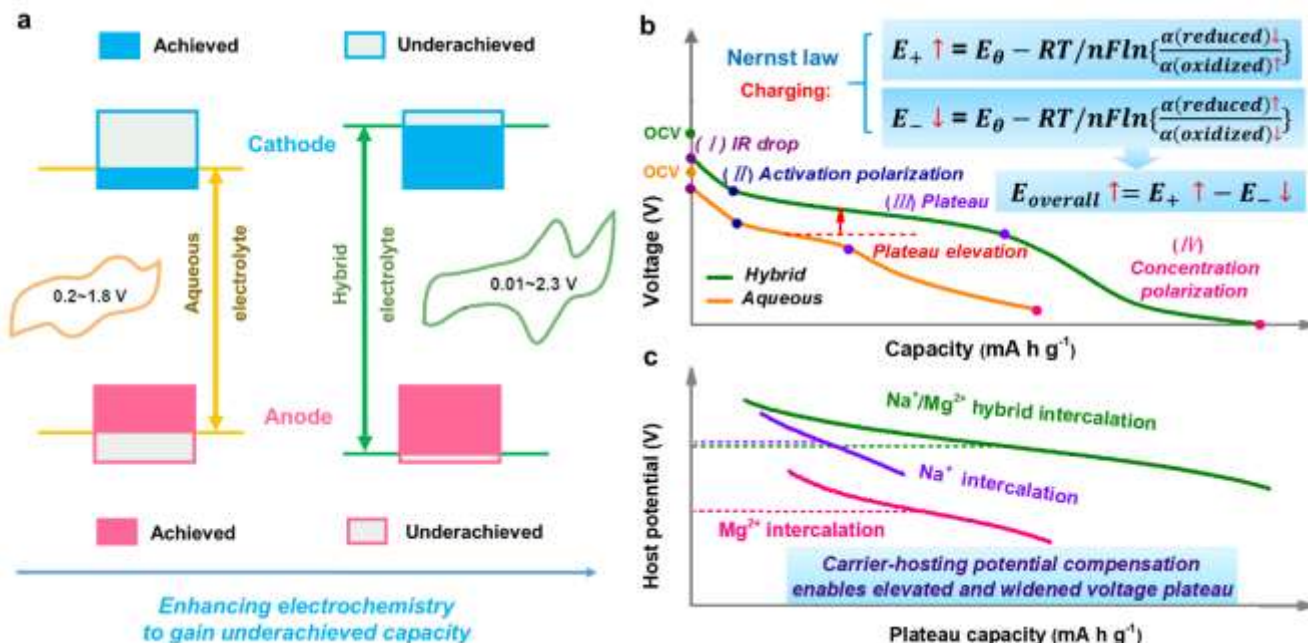
**Scheme 1**. (a) Illustration of the origin of the underachieved capacity of the electrodes in a conventional aqueous electrolyte, and the potential strategy of enhancing the electrochemical process to gain the underachieved capacity; (b) illustration of the key role of a high operation voltage in achieving a high capacity/voltage; (c) illustration of the principle of carrier-hosting potential compensation, enabling an elevated and widened voltage plateau.

High-voltage electrolytes play a key role in achieving a strong electrochemical process by overcoming the relatively high reaction energy barriers.[5] For certain (de)intercalated-type electrode materials with stable structure, when a higher the operation voltage is adopted, more (de)intercalated charge carriers will be involved in the reactions. The operation voltage of ~2 V achieved in conventional aqueous electrolytes is still inadequate for realizing sufficient intercalation/de-intercalation of charge carriers. This usually results in an underachieved specific capacity (**Scheme 1a**).[5b, 6] Recently, aqueous/organic hybrid electrolytes are demonstrated to elevate the operation voltage of supercapacitors and batteries.[7] The introduction of organic cosolvents (acetonitrile, dimethyl carbonate, etc.) can easily increase the operating voltage of hybrid electrolytes to 2.2–2.5 V, which is higher than those of most conventional aqueous electrolytes.[8] Encouragingly, the appropriately introduced organic cosolvents do not significantly compromise the fast dynamics of aqueous electrolytes, thus providing considerable opportunities to exploit new battery chemistries. The relationship between the amount of (de)intercalated charge carrier and electromotive force of electrode materials confirms to Nernst's law: $E = E_\theta - RT/nFln\{\frac{\alpha(reduced)}{\alpha(oxidized)}\}$, where $E$ and $E_\theta$ is real and standard electromotive force, respectively. $n$ is charge number transferred, $F$ is Faraday constant, and $\alpha$ is activity of reduced or oxidized components. During the charging process, $\alpha(reduced)$ decreases while $\alpha(oxidized)$ increases gradually, resulting in the increase of electromotive force of cathode ($E_+$). Simultaneously, anode material experiences an inverse change in the ratio of $\frac{\alpha(reduced)}{\alpha(oxidized)}$, leading to the decrease of electromotive force of anode ($E_-$). Thus the open circuit voltage of battery ( $E_{overall} = E_+ - E_-$ ) increases with the increase of (de)intercalated charge carrier amount enabled by high operation voltage. After deducting the IR drop and polarizations

(activation- and concentration-polarization), an elevated voltage plateau could be achieved (**Scheme 1b**). In addition, the inherent intercalation chemistry and hosting potentials of electrode materials also matter in achieving high-voltage/capacity hybrid batteries.[9] For divalent $Mg^{2+}$-involved battery systems, a strong Coulomb repulsion force from host lattice atoms is the main origin of severe electrochemical polarization. This generally results in discharge voltage plateaus below 1.00 V and low capacity of aqueous magnesium-ion batteries.[10] In contrast, with a relatively low cost and small migration barrier, the intercalation chemistry of monovalent $Na^+$ carriers proceeds much more easily in host materials.[11] The smaller polarization of $Na^+$ (de)intercalation usually affords a higher hosting potential in electrodes compared to the case of $Mg^{2+}$ (de)intercalation. In this regard, the hybrid (de)intercalation of $Mg^{2+}/Na^+$ enables faster reaction kinetics and more available carriers than single $Mg^{2+}$ (de)intercalation chemistry, which underlies a potentially higher voltage and capacity (**Scheme 1c**).

Currently, despite some efforts devoted to hybrid intercalation chemistry, the obtained voltage plateau and specific capacity remain unsatisfactory. For the hybrid $Mg^{2+}/Na^+$ storage, the voltage plateau is mostly below 1.20 V and the energy density is approximately 40–70 Wh kg$^{-1}$, which cannot meet the requirements of high-energy devices.[1a, 1c, 12] The low voltage plateau mainly results from the relatively low operation voltage (~1.80 V) of the aqueous electrolyte. Although with a higher operation voltage, the full cells in organic electrolytes generally suffer from intrinsically sluggish kinetics, which hinders the enhancement of the electrochemistry. Fortunately, aqueous/organic hybrid electrolytes inherit fast dynamics and a wide voltage window from aqueous and organic electrolytes, respectively, enabling a high voltage plateau and high capacity. To date, aqueous/organic hybrid electrolytes have not been employed for $Mg^{2+}/Na^+$ hybrid batteries. Additionally, the typical cathodes for aqueous $Mg^{2+}$ storage, including manganese

2

oxides and $Mg^{2+}$-intercalated manganese oxides, still suffer from intractable dissolution and collapse issues. As an unprecedented phase, $Mg_{1.5}VCr(PO_4)_3$ phase (MVCP) is insoluble in aqueous electrolytes and capable of hosting charge carriers, similar to previously reported $Li_3V_2(PO_4)_3$ phase.[2a] Due to the intrinsically Mg-containing trait, MVCP possesses good structural stability to endure lattice strain with the (de)intercalation of charge carriers. The relatively low conductivity of MVCP can be overcome by combining with highly conductive carbon materials for enhanced electrochemical performance. Such properties of MVCP make it promising for aqueous high-voltage $Mg^{2+}/Na^+$ hybrid batteries, which, however, has not been exploited. For such hybrid battery systems, in-depth mechanistic insight into the hybrid intercalation chemistry of charge carriers and voltage plateau elevation remains extremely scarce.

In this study, with a new aqueous/organic $Mg^{2+}/Na^+$ hybrid electrolyte, unprecedented MVCP is employed as the cathode to couple with $FeVO_4$ (FVO) anode, realizing a high voltage plateau of ~1.50 V and capacity that is ≥1.75-fold higher than those in conventional aqueous electrolytes. After 1350 cycles at 1 A g$^{-1}$, the full cell still delivered a well-retained voltage plateau, showing a low capacity decay of 0.018% per cycle. The high operation voltage allowed by the hybrid electrolyte makes the (de)intercalation electrochemistry more sufficient, contributing to the enhanced capacity (**Scheme 1a-b**). With a relatively high hosting potential, $Na^+$-intercalation in the electrodes fills the low-potential drawback of $Mg^{2+}$ (de)intercalation, synergistically widening and elevating the discharge plateau of the full battery (**Scheme 1c**). Mechanism study shows that FVO unusually transforms into the $Fe_2V_3$ phase, while MVCP exhibits pseudocapacitive-(de)intercalation behaviors with low lattice strain. The as-assembled full battery initiated a high pseudocapacitive proportion of over 67.3%. This work demonstrates an advisable strategy towards high-energy batteries by enhancing the electrochemistry with carrier-hosting potential compensation, which could promote the development of other advanced aqueous hybrid batteries.

## Results and Discussion

### *Lattice architecture and materials characterization*

The MVCP was obtained as a cathode material by a solid-phase thermochemical method (Experimental Section, Supporting Information). **Figure 1a** shows the Rietveld refined X-ray diffraction (XRD) pattern of MVCP, where the diffraction peaks match well with the single $Mg_{1.5}VCr(PO_4)_3$ phase. The Cr doping ratio was calculated to be ~48.2% based on the atomic ratio of Cr to (Cr + V). The mixed degree between Cr and V in
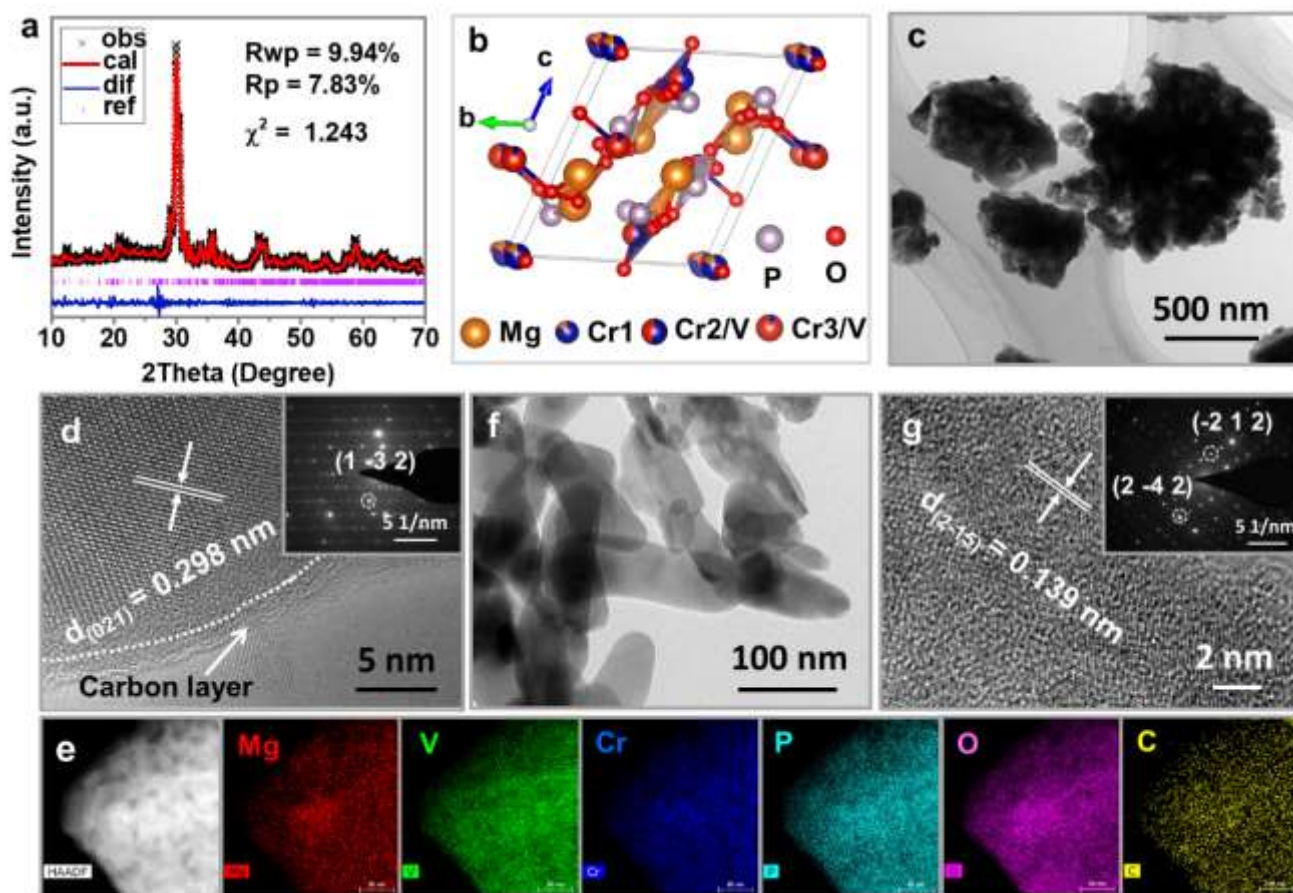


**Figure 1.** (a–b) Rietveld refined XRD pattern of MVCP and the corresponding lattice architecture of MVCP; (c–d) TEM and HR-TEM images of MVCP (inset shows the corresponding SAED pattern); (e) EDS elemental mapping of MVCP, including Mg, V, Cr, P, O, and C; (f–g) TEM and HR-TEM images of FVO (inset shows the corresponding SAED pattern).

3

the lattice is ~0.933, which was calculated based on the occupancy ratio of Cr to V. **Figure 1b** exhibits the lattice architecture of MVCP, which can be assigned to the cubic symmetry within the space group P-1 ($a$ = 6.269815 Å; $b$ = 7.912693 Å; and $c$ = 9.244180 Å; **Table S1**). The corresponding atomic sites are listed in **Table S2**. The scanning electron microscopy (SEM) image revealed a micro-sized particle morphology of the obtained MVCP sample (**Figure S1**). The Raman spectrum shows two typical bands at 1361 and 1599 cm$^{-1}$, which correspond to the D- and G-bands of the precursor-derived carbon (**Figure S2a**).[13] Transmission electron microscopy (TEM) images showed that the microparticles are formed with the assembly of secondary nanoparticles, which could result from the solid-phase reaction process during the material synthesis (**Figure 1c**). As shown in **Figure 1d**, the high-resolution transmission electron microscopy (HR-TEM) image exhibits the presence of carbon layers and an interplanar spacing of 0.298 nm, corresponding to the (0 2 1) lattice plane of the MVCP. In addition, the (1 -3 2) lattice plane appears in the well-defined selected area electron diffraction (SAED) pattern, where some evident light spots could be associated with lattice

distortion from the mutual substitution of Cr and V atoms (inset). Corresponding to the high-angle annular dark-field (HADDF) image, energy-dispersive X-ray spectroscopy (EDS) elemental mapping displays a matched distribution of Mg, V, Cr, P, O, and C **(Figure 1e)**. Additionally, through a facile hydrothermal synthesis, followed by annealing, FVO was fabricated as the anode material (Experimental Section, Supporting Information). The XRD pattern shows well-defined diffraction peaks, which are consistent with the standard phase (JCPDS No. 38-1372, **Figure S3a**). The lattice architecture of FVO is exhibited in **Figure S3b**. The corresponding Raman spectrum displays the featured bands, which are associated with terminal V–O stretching, bridging V–O··Fe stretching, and V–O–V deformations/Fe–O stretching, respectively (**Figure S4**).[14] The SEM and TEM images present a rod-like structure of FVO (**Figure S5**, **Figure 1f**), and **the** corresponding EDS elemental mapping shows a well-matched distribution **(Figure S6)**. The HR-TEM image displays a representative interplanar spacing of 0.139 nm, which is assigned to the lattice plane (2 -1 5) of FVO (**Figure 1g**). The SAED pattern (inset) clearly shows the diffraction spots corresponding to the lattice plane (2 -4 2) and (-
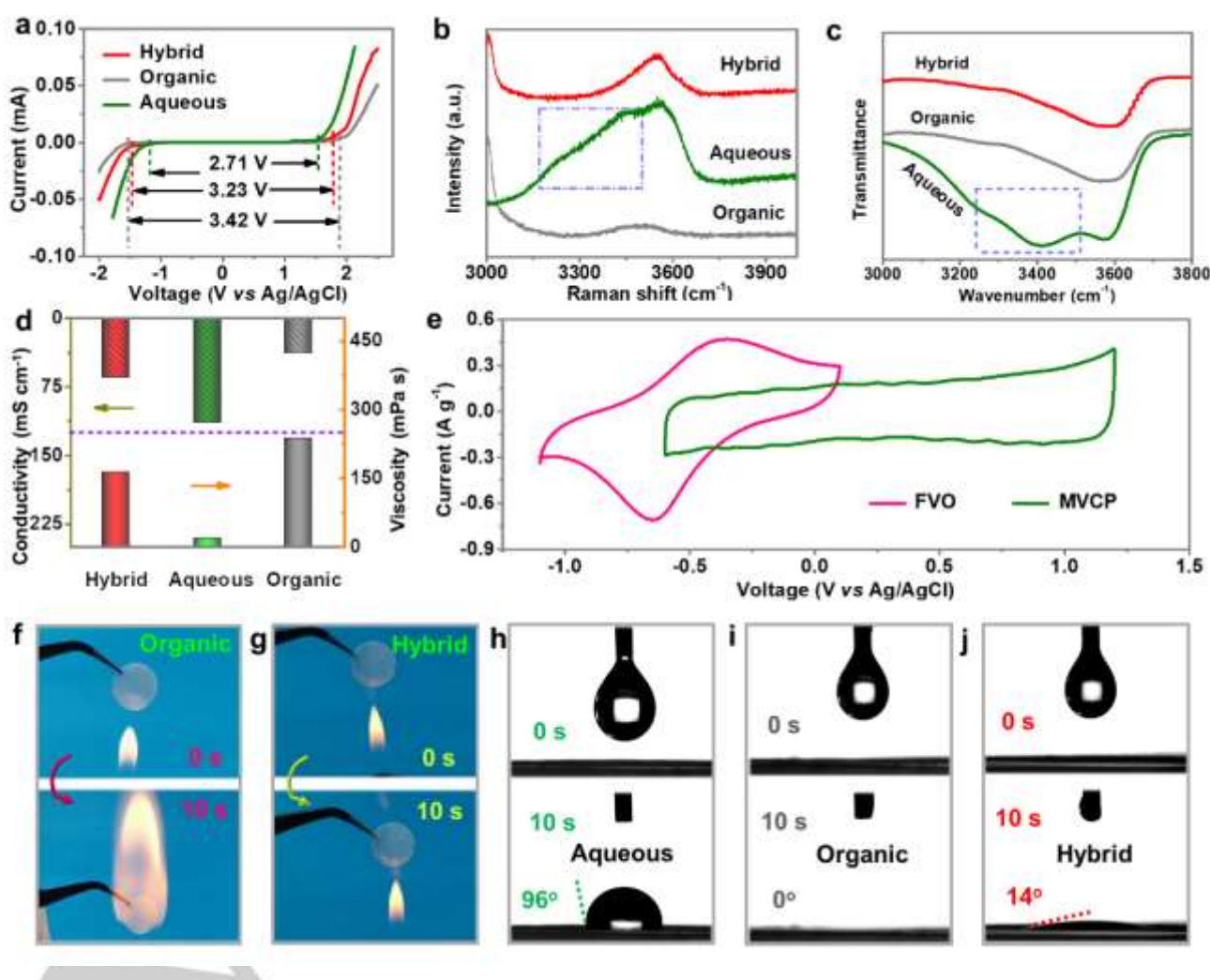


**Figure 2.** (a) LSV curves showing the voltage windows of different electrolytes; (b) Raman spectra and (c) FT-IR spectra of different electrolytes; (d) the ionic conductivity and viscosity measurements of different electrolytes; (e) CV curves of half cells in the hybrid electrolyte, with FVO and MVCP as working electrodes; (f–g) ignitability demonstration of the hybrid electrolyte and organic (AN) electrolyte; (h–j) contact angle tests of different electrolytes on the surface of the electrode.

4

2 1 2).

### Electrochemical analysis of hybrid electrolytes

To investigate the effect of a high operation voltage on the battery performance, a hybrid electrolyte with acetonitrile (AN) and deionized water as cosolvents was employed. The volumetric ratio of AN to deionized water in all the hybrid electrolytes was fixed at 4.1:0.9 to guarantee good non-flammability. Sodium perchlorate was employed as the main solute in the hybrid electrolyte to stabilize free $H_2O$ molecules, aiming to reduce the water splitting under a high voltage. Magnesium perchlorate was utilized to afford a sufficient $Mg^{2+}$ carrier. As shown in **Figure 2a**, the optimized hybrid electrolyte with an $Na^+$ to $Mg^{2+}$ molar ratio of 6:0.5 typically displays a 3.23-

V voltage window, which is wider than those of the hybrid electrolytes with other ratios (such as 5:0.75 and 6.75:0.25, **Figure S7**). Such a voltage window is significantly wider than that of the aqueous electrolyte (2.71 V) and close to that of pure AN solution (3.42 V). The Raman band ranging from 3100 to 3500 $cm^{-1}$ in the hybrid electrolyte disappears, corresponding to the weakening of the O–H stretching vibration, verifying that most of the free water molecules were well-stabilized **(Figure 2b)**.[7b] This result benefits from the complexation of high-concentrated $Na^+$ with $H_2O$ molecules and mutual hydrogen bonding between $H_2O$ and AN molecules. It accounts for the enhancement of the operation voltage of hybrid electrolytes. As shown in **Figure 2c**, after hybridization with an organic solvent, the featured Fourier transform infrared spectroscopy (FT-IR) peak (dotted box) related to aggregated $H_2O$ molecules by
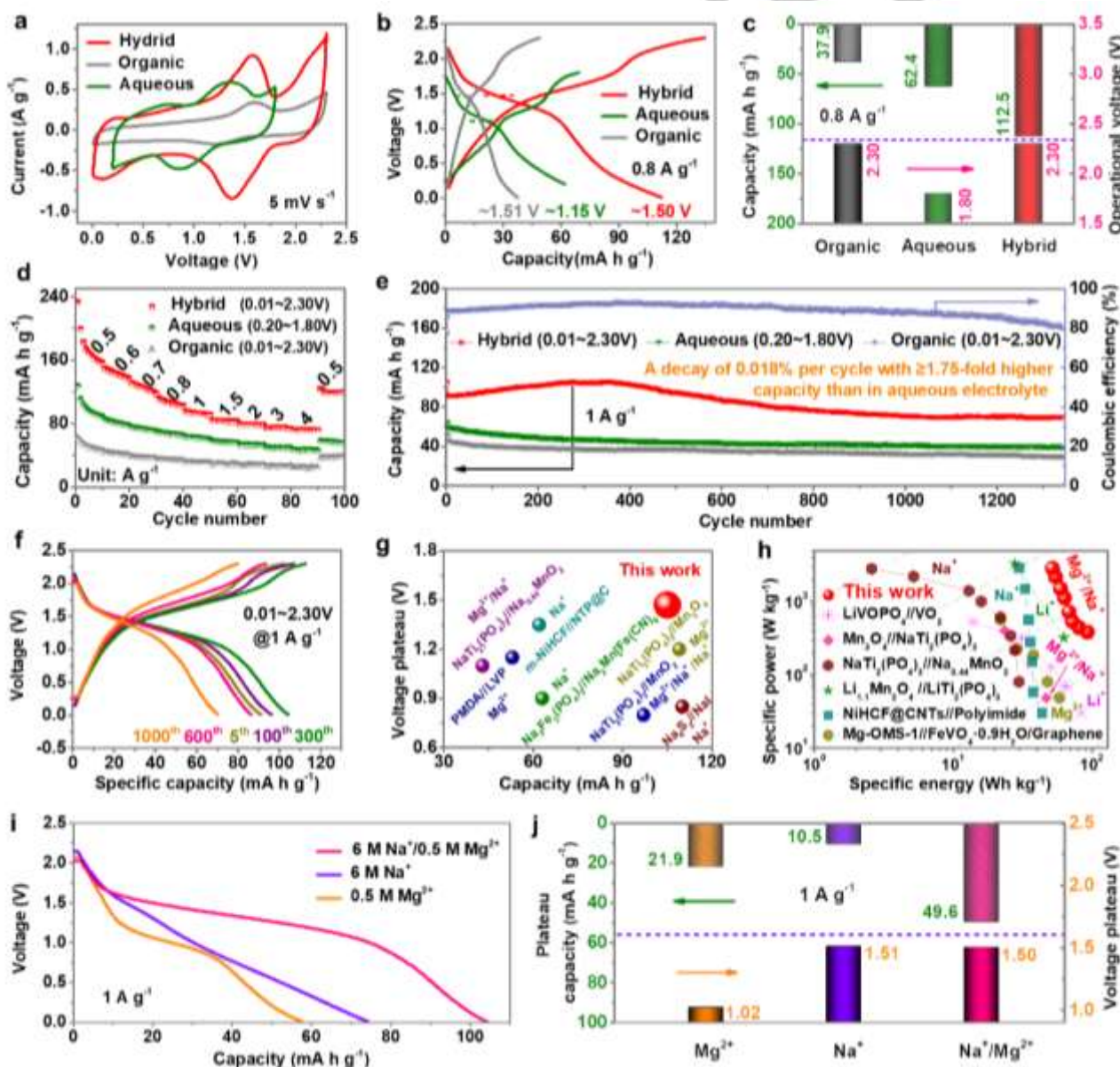


**Figure 3.** Electrochemical properties of the full cells in different electrolytes: (a) CV curves; (b) rate capability; (c) charge–discharge curves; (d) long-life cyclability; (e) charge–discharge curves in hybrid electrolytes with different cycles; (f) voltage plateau comparison of the full cells in the hybrid electrolyte with previously reported aqueous $Mg^{2+}$, $Na^+$, and $Mg^{2+}/Na^+$ hybrid battery systems; (g) voltage plateau and capacity comparison of various batteries; (h) Ragone plot comparison of the full cell in the hybrid electrolyte with other aqueous batteries; (i) discharge curves of the full cells in different hybrid electrolytes; (j) histogram exhibiting the plateau capacity and voltage plateau of the full cells in various hybrid electrolytes.

5

hydrogen bonds disappeared, which further suggests the decrease in free $H_2O$ in the hybrid electrolyte.[7b] As shown in **Figure 2d**, compared with the organic electrolyte, the hybrid electrolyte delivers an improved ionic conductivity and viscosity, which contribute to obtaining fast electrochemical kinetics. The cyclic voltammetry (CV) curves of the half cells in a three-electrode system exhibit rational profiles, indicating the good operability of the optimized hybrid electrolyte (**Figure 2e**). Compared with the organic solution, the ignitability tests demonstrate a good non-flammability of the hybrid electrolyte, which is conducive for obtaining highly safe batteries (**Figure 2f-g**). The contact angle tests on the prepared electrodes show the superior wettability of the hybrid electrolyte to the aqueous electrolyte, which contribute to achieving a high-rate capability (**Figure 2h-j**).

### *Electrochemical property tests*

The electrochemical properties were studied by testing the full cells in different electrolytes. As shown in **Figure 3a**, when scanned at 5 mV s⁻¹, the CV curve for the hybrid electrolyte displays higher peak potentials than those for the aqueous and organic (AN) electrolytes. This indicates that a relatively high voltage plateau can be achieved. The galvanostatic discharge/charge tests were conducted at different cut-off voltages: 0.01–2.30 V for the hybrid and organic (AN) electrolytes, and 0.20–1.80 V for the aqueous electrolyte. As shown in **Figure 3b**, the hybrid electrolyte contributes to achieving a high voltage plateau of 1.50 V and a capacity of 112.5 mA h g⁻¹ at 0.8 A g⁻¹. In contrast, in the aqueous electrolyte, the full cell only exhibits a low voltage plateau of 1.15 V and a low capacity of 62.4 mA h g⁻¹ at 0.8 A g⁻¹, which is disadvantageous for achieving a high energy density. In the organic electrolyte, the full cell delivers a voltage plateau of 1.51 V voltage plateau but an extremely low capacity of 37.9 mA h g⁻¹ at 0.8 A g⁻¹, which is associated with the intrinsically sluggish electrochemical kinetics.[9b] **Figure 3c** shows the corresponding correlation between the operation voltage and capacity in various electrolytes. Impressively, with the well-inherited fast kinetics from the aqueous electrolyte and high operation voltage from the organic electrolyte, the hybrid electrolyte shows overwhelming merits in the simultaneous realization of high voltage/capacity. These results confirm to Nernst's law, emphasizing the importance of enhancing the electrochemical processes by elevating the operation voltage for realizing high specific energy (**Scheme 1b**). **Figure 3d** further shows the rate capability of the full cells in various electrolytes, where the hybrid electrolyte exhibited significantly high performance in aqueous and organic (AN) electrolytes. The corresponding discharge/charge curves in the hybrid electrolyte are shown in **Figure S8**, where the voltage plateaus are well-retained at different current densities. For comparison, the rate capability in small cut-off voltages (0.01–2.20 V and 0.01–2.10 V) was evaluated in the hybrid electrolyte (**Figure S9**). Compared with that at a cut-off voltage of 0.01–2.30 V, both the discharge plateaus and capacity are lowered, validating the positive effect of a high operation voltage on the energy density of the batteries (**Figure S10**).

When cycled at 1 A g⁻¹ after 1350 cycles, the full cell in the hybrid electrolyte still delivers a significantly higher capacity than those in aqueous and AN electrolytes, with a low decay rate of 0.018% per cycle, as shown in **Figure 3e**. In particular, a high capacity of 104.7 mA h g⁻¹ is obtained in the hybrid electrolyte, which is ≥1.75-fold higher than that in the aqueous electrolyte (57.8 mA h g⁻¹). In addition, the discharge/charge curves corresponding to the 5ᵗʰ, 300ᵗʰ, 600ᵗʰ, and 1000ᵗʰ cycles still present evident voltage plateaus of ~1.3 V, suggesting a stable voltage output (**Figure 3f**). Compared with the previously reported $Mg^{2+}$, $Na^+$, and $Mg^{2+}/Na^+$ hybrid battery systems, the 1.5-V high voltage plateau of full cell in hybrid electrolyte also exhibits a remarkable advantage (**Figure 3g**, **Table S3**).[2a, 15] Based on the mass of the electrode (m), the energy density and power density of the full cells were calculated following the equations: $E = \int_0^t iV/m \ \mathrm{dt}$ and $P = \frac{1}{t}\int_0^t iV/m \ \mathrm{dt}$, respectively, where $i$, $v$, and $t$ represent the current, voltage, and discharge time, respectively. As shown in **Figure 3h**, the Ragone plot of the full cell in the hybrid electrolyte exhibits an excellent advantage over the other typical aqueous batteries with different carriers (e.g. $Mg^{2+}$, $Na^+$, $Li^+$, and $Mg^{2+}/Na^+$; **Table S4**),[15d, 16] specifically with an energy density of 92.7 Wh kg⁻¹electrode and a power density of 2.88 kW kg⁻¹electrode.

The mechanism of the voltage plateau enhancement was further investigated by decoupling the $Mg^{2+}/Na^+$-intercalation chemistry of the full cells. In the hybrid electrolyte containing only $Na^+$ or $Mg^{2+}$ carriers, both the full cells show a couple of evidently weakened redox peaks, compared with those with both $Na^+/Mg^{2+}$ carriers (**Figure S11**). As shown in **Figure 3i**, the discharge–charge curves at 0.8 A g⁻¹ exhibit average voltage plateaus of 1.50, 1.51, and 1.02 V in $Mg^{2+}/Na^+$, $Na^+$, and $Mg^{2+}$ electrolytes, respectively. Correspondingly, the plateau capacities are 48.9, 10.5, and 21.9 mA h g⁻¹ in $Mg^{2+}/Na^+$, $Na^+$, and $Mg^{2+}$ electrolytes, respectively (**Figure 3j**). These results demonstrate an evident potential compensation effect between $Na^+$- and $Mg^{2+}$-intercalations in the hybrid $Mg^{2+}/Na^+$ electrolyte (**Scheme 1c**). Benefiting from this effect, the voltage plateau in the $Mg^{2+}/Na^+$ hybrid electrolyte is higher and wider than those in the $Na^+$- and $Mg^{2+}$-containing electrolytes, resulting in an increased capacity. Moreover, the full cells with $Mg^{2+}/Na^+$ hybrid intercalation chemistry deliver a superior rate capability compared to those with only $Mg^{2+}$ or $Na^+$-intercalation (**Figure S12**). The hybrid $Mg^{2+}/Na^+$-intercalation also evidently improves battery stability (**Figures S13–14**). These results verify that enhancing the electrochemistry with carrier-hosting potential compensation synchronously enhances the voltage plateau and reversible capacity.
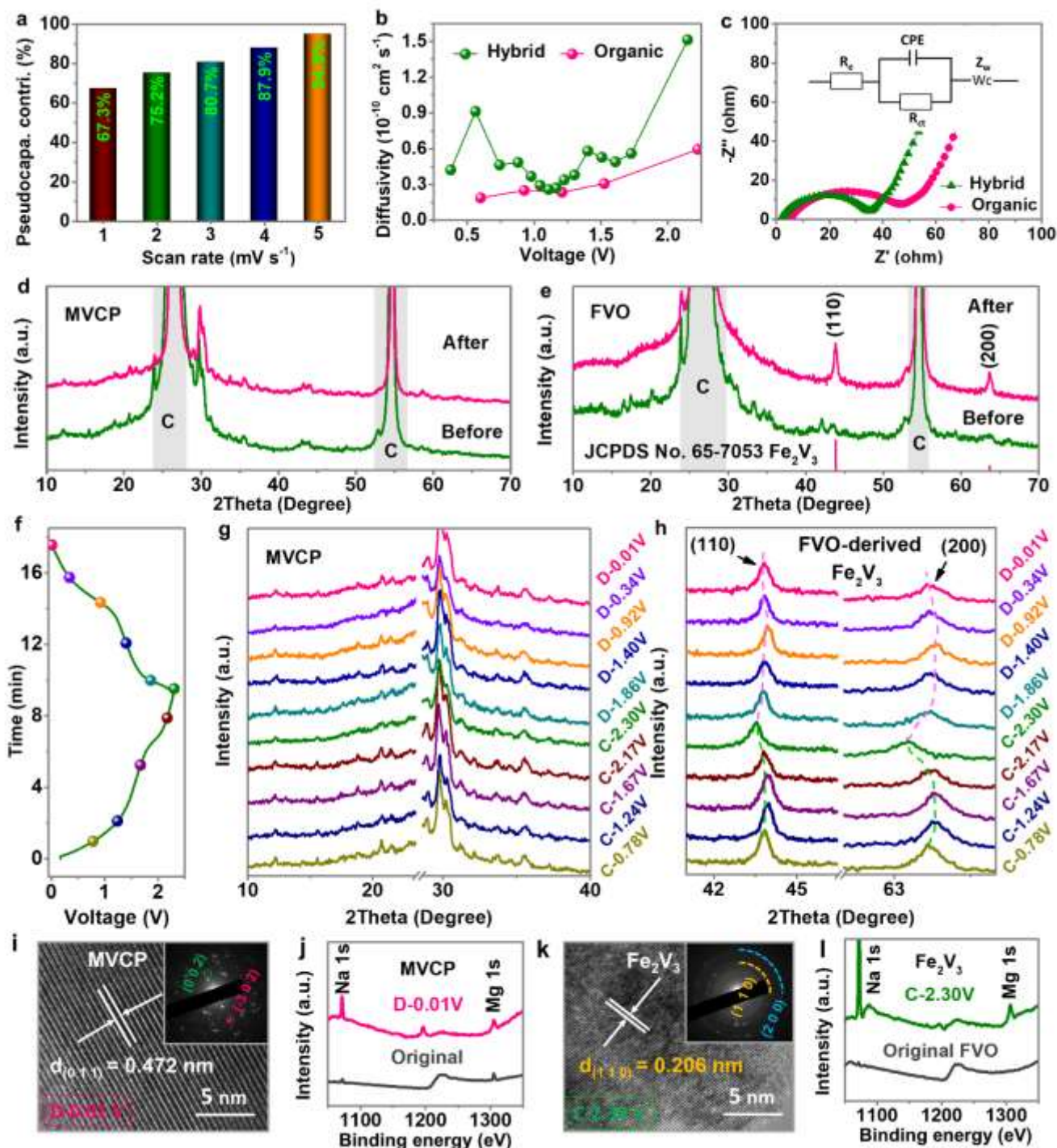
### *Electrochemical kinetics and mechanism study*

The pseudocapacitive effect in the full cell was evaluated according to the CV curves at various scan rates (**Figure S15a**). Based on the following equation: $i = av^b$, where $i$ is the peak current, and $a$ and $b$ are constants, the $b$ value can be obtained to qualitatively evaluate the pseudocapacitive contribution.[17] Corresponding to the two redox peaks in the CV curves, the fitted $b$ values are 0.916 and 0.917, indicating the presence of a considerable pseudocapacitive proportion (**Figure S15b**). The specific contribution was calculated using the following equation: $i = k_1 v + k_2 v^{1/2}$, where $k_1$ and $k_2$ are constants, and $v$ is the scan rate.[18] As shown in **Figure 4a**, the full cell in the hybrid electrolyte exhibits high pseudocapacitive contributions at scan rates of 1, 2, 3, 4, and 5 mV s⁻¹, which are 67.3%, 75.2%, 80.7%, 87.9%, and 94.8%, respectively. Representatively, the CV curve

6

at 3 mV s$^{-1}$ and the corresponding pseudocapacitive contribution (shaded part) are shown in **Figure S16**. To investigate the influence of the H$_2$O molecules in the hybrid electrolyte on the electrochemical kinetics, the diffusion coefficient was further measured by the galvanostatic intermittent titration technique (GITT). The GITT curve of the full cell in the hybrid electrolyte

demonstrates an evident discharge plateau, while in the AN electrolyte, it is difficult to be observed, which is associated with the higher desolvation barrier (**Figure S17**).[9b] The single GITT titration profile in the hybrid electrolyte is displayed in **Figure S18a**. Correspondingly, the fitted voltage vs. discharge time ($\tau$)$^{1/2}$ plot shows good linearity (**Figure S18b**), indicating that the



**Figure 4.** (a) Pseudocapacitive contribution (Pseudocapa. contri.) distribution of the full cell at various scan rates; (b) diffusion coefficient distribution of the full cells in hybrid and AN electrolytes based on GITT discharge profiles; (c) Nyquist plots of the full cells in different electrolytes (inset shows the corresponding equivalent circuit). (d–e) XRD patterns of MVCP and FVO in the full cells before and after cycling; (f) discharge–charge-time curves of the full cells for the mechanism study; (g–h) *ex situ* XRD patterns of MVCP and FVO at corresponding voltages; (i) HR-TEM images of the cycled MVCP discharged to 0.01 V; (j) in-depth XPS survey of the cycled MVCP discharged to 0.01 V; (k) HR-TEM images of the cycled FVO charged to 2.30 V; (l) in-depth XPS survey of the cycled FVO charged to 2.30 V.

7

diffusion coefficient (*D*) can be calculated according to the equation:[19]

$$D = \frac{4}{\pi\tau}(\frac{mV_m}{MA})^2(\frac{\Delta E_S}{\Delta E_\tau})^2 \ (\tau \ll L^2/D) \qquad (1)$$

where m, $V_m$, and M are the mass, molar volume, and molecular weight of the active material, respectively, and A is the total surface area of the electrode. As shown in **Figure 4b**, the full cell in the hybrid electrolyte generally delivers a higher diffusivity than that in the AN electrolyte, verifying the key role of $H_2O$ molecules in boosting electrochemical kinetics. Electrochemical impedance spectroscopy (EIS) was employed to probe the charge-transfer resistance of the full cells in different electrolytes **(Figure 4c)**. The inset shows the equivalent circuit corresponding to the Nyquist curves, where $R_e$, $R_{ct}$, $Z_w$, and CPE represent the ohm resistance between the electrolyte and electrode, charge-transfer resistance, Warburg impedance related to the ionic diffusion, and double-layer capacitance and passivation film capacitance, respectively.[20] In the middle-frequency region, the full cell in the hybrid electrolyte possesses a smaller semicircle diameter than that in the AN electrolyte, implying a promoted charge transfer in the presence of water.

The electrochemical mechanisms of the electrode materials were further revealed by *ex-situ* XRD. As shown in **Figure 4d**, after cycling, MVCP shows no noticeable phase change. Interestingly, the XRD patterns of cycled FVO show a marked phase transition with the formation of an intermetallic phase of $Fe_2V_3$ (JCPDS No. 65-7053, **Figure 4e**). Corresponding to the discharge/charge curve in **Figure 4f**, the anode and cathode materials in different charge/discharge states were further carefully characterized by *ex-situ* XRD. As shown in **Figure 4g**, throughout the discharge–charge process, MVCP displays no noticeable diffraction peak shift, implying the presence of a low lattice strain. In contrast, for the FVO-derived $Fe_2V_3$ phase, reversible diffraction peak shifts appear in the (1 1 0) and (2 0 0) lattice planes, which could be associated with the

electrochemical combination between $Fe_2V_3$ and $Mg^{2+}/Na^+$ carriers (**Figure 4h**). This phenomenon has never been reported in aqueous sodium/magnesium-ion batteries.

The morphological evolution of electrode materials in fully charged/discharged states was further characterized by TEM. Compared with the original sample, the fully discharged/charged MVCP shows no evident differences in morphology and in the EDS elemental mapping (**Figure S19**). The HR-TEM image of MVCP discharged to 0.01 V, as shown in **Figure 4i,** clearly presents a typical lattice plane of (0 1 1) with an interplanar spacing of 0.472 nm. The SAED pattern (**inset**) shows the presence of different lattice planes, such as (0 0 2) and (-3 0 2). To study the (de)intercalation processes of $Mg^{2+}$ and $Na^+$, the cycled electrode materials were further characterized by *ex-situ* in-depth X-ray photoelectron spectroscopy (XPS) and TEM. As shown in **Figure 4j**, compared with the original MVCP, when discharged to 0.01 V (carrier-intercalated state), the cycled MVCP shows featured in-depth XPS peaks of Mg 1s and Na 1s, verifying the co-intercalation of $Mg^{2+}/Na^+$ carriers in MVCP. Additionally, the cycled anode material retains the original rod-like morphology, and EDS elemental mapping corresponding to the sample discharged to 0.01 V shows the uniform distribution of Fe and V (**Figure S20**). The HR-TEM image exhibited an interplanar spacing of 0.206 nm, corresponding to the (1 1 0) lattice plane of FVO-derived $Fe_2V_3$. The SAED pattern exhibits two noticeable diffraction circles, which are indexed to the (1 1 0) and (2 0 0) lattice planes of FVO-derived $Fe_2V_3$, respectively (**Figure 4k**). As shown in **Figure 4l**, compared with the original FVO, the in depth XPS survey of the anode (FVO-derived $Fe_2V_3$) charged to 2.30 V (carrier-intercalated state) shows Na 1s and Mg 1s peaks, confirming the co-intercalation of $Mg^{2+}/Na^+$ carriers in FVO-derived $Fe_2V_3$. The effects of different charge carriers on electrochemical behavior of electrode materials were further decoupled. In $Na^+$-containing hybrid electrolyte, the CV curve of MVCP cathode presents a jagged profile, indicating a
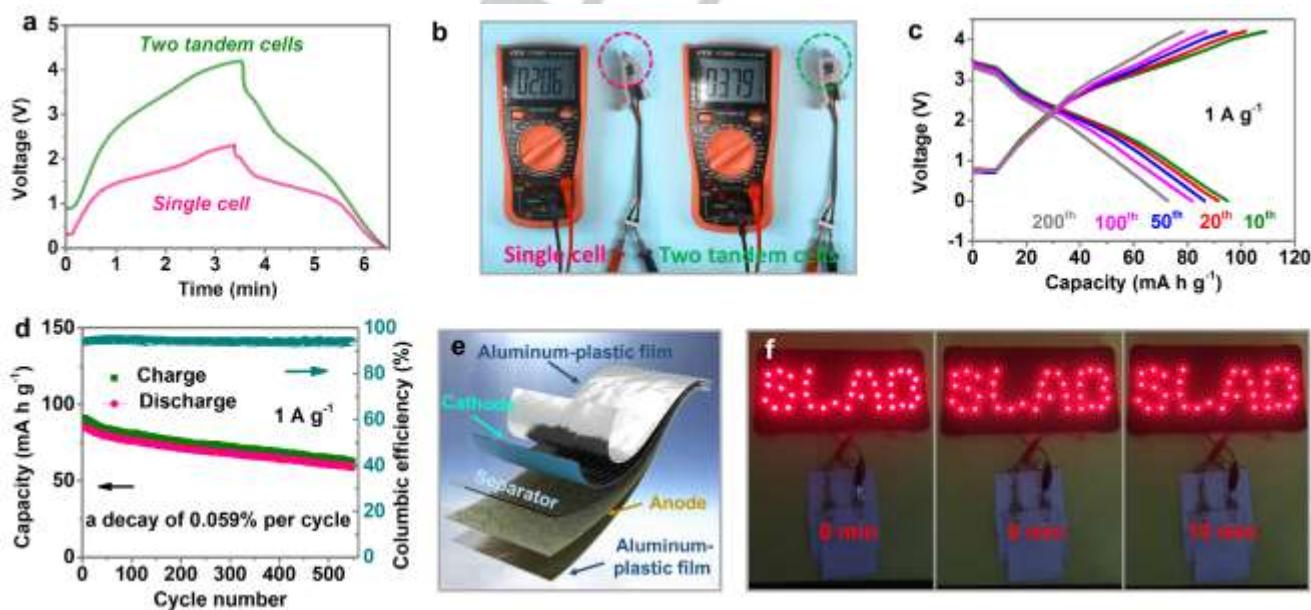
**Figure 5.** (a) Discharge–charge-time curves of a single coin cell and two tandem coin cells; (b) open-circuit voltage of a single coin cell and two tandem coin cells; (c) discharge–charge curves of two tandem coin cells at different cycles; (d) long-life cycling performance of two tandem coin cells at 1 A g$^{-1}$; (e) schematic illustration of a pouch cell; (f) digital photograph showing 35-LED bulb patterns powered by two tandem pouch cells.

8

pseudocapacitive (de)intercalation behavior; while in Mg$^{2+}$-containing hybrid electrolyte, MVCP cathode exhibits a quasi-capacitive behavior (**Figure S21**). By contrast, the CV curves of FVO anode display evident redox peaks in both Na$^+$- and Mg$^{2+}$-containing hybrid electrolytes, featuring a typical (de)intercalation behavior of battery (**Figure S22**). These imply that the battery behavior of full cell in hybrid electrolytes results from synergistic co-(de)intercalation of Mg$^{2+}$/Na$^+$ carriers.

To evaluate the amount of Mg$^{2+}$ and Na$^+$ inserted into MVCP cathode and FVO anode, the cycled electrode materials were characterized by inductively coupled plasma mass spectrometry (ICP-MS) and SEM-EDS. Previously, similar methods have been used for the determination of the carrier-intercalated amount into vanadium oxides.[21] According to the ICP-MS results in **Table S5**, the intercalated amount of Mg$^{2+}$ and Na$^+$ in 1 FVO-derived anode is *ca.* 0.32 and 0.90, respectively. The intercalated amount of Mg$^{2+}$ and Na$^+$ in 1 MVCP cathode is *ca.* 0.35 and 0.65, respectively. The theoretical capacity corresponding to the Mg$^{2+}$/Na$^+$-intercalated amount in MVCP is *ca.* 85.2 mA h g$^{-1}$ at 1 A g$^{-1}$, which is close to the measured capacity in **Figure 3e**. Also, the ICP-MS analysis further verifies the co-intercalation of Mg$^{2+}$/Na$^+$ in MVCP cathode and FVO-derived anode.

***Electrochemical performance of tandem full cells***

To inspect the practicality of the full cells in the hybrid electrolyte, the electrochemical performances of cascaded cells were comparatively studied.[22] As shown in **Figure 5a**, two tandem cells work effectively at 1 A g$^{-1}$ with a discharge voltage plateau of ~2.40 V. **Figure 5b** displays the digital photographs of the fully charged single cell and two tandem cells, with high open-circuit voltages of 2.09 and 3.79 V, respectively. Particularly, the voltage plateau of the two tandem cells at ~2.40 V is well-retained for the 10$^{th}$, 20$^{th}$, 50$^{th}$, 100$^{th}$, and 200$^{th}$ cycles, featuring a stable voltage output of tandem cells (**Figure 5c**). A high reversible capacity of 91.8 mA h g$^{-1}$ is obtained, showing a low decay of 0.059% per cycle after 550 cycles (**Figure 5d**). A large pouch cell with a dimension of 4 × 5 cm$^2$ was further assembled to inspect its powering ability. **Figure 5e** schematically illustrates the typical configuration of the pouch cell. As displayed in **Figure 5f**, two tandem pouch cells power a large light-emitting diode (LED) panel "SLAB" composed of 35 bulbs for over 10 min, evidencing the excellent scalability of the full cell.

## Conclusion

While featuring high safety and low cost, the development of aqueous magnesium-ion full batteries remains hindered by their low voltage plateau and low capacity. In this study, with new aqueous/organic Mg$^{2+}$/Na$^+$ hybrid electrolytes, an unprecedented MVCP is initially employed as the cathode and coupled with the FVO anode, realizing a high voltage plateau of ~1.50 V and a capacity (233.4 mA h g$^{-1}$ at 0.5 A g$^{-1}$, 92.7 Wh kg$^{-1}$$_{electrode}$) that is ≥1.75-fold higher than those in conventional aqueous electrolytes. The high operation voltage allowed by the hybrid electrolyte realizes enhanced (de)intercalation of charge carriers, which enhances the capacity remarkably. With a relatively high hosting potential, Na$^+$ (de)intercalation in the

electrodes effectively compensates the low-potential drawback of Mg$^{2+}$ (de)intercalation, synergistically elevating and widening the discharge plateau of the full battery. After 1350 cycles at 1 A g$^{-1}$, the full cell delivered a low capacity decay of 0.018% per cycle, with a well-retained voltage plateau. Mechanism study further unveils that FVO unusually transforms to Fe$_2$V$_3$ phase in the initial electrochemical process, which acts as a new anode host for hybrid Mg$^{2+}$/Na$^+$ storage. With a low lattice strain, the MVCP cathode features pseudocapacitive-intercalation chemistry. The as-assembled full battery exhibits a pseudocapacitive proportion of more than 67.3%. By enhancing the electrochemistry with the carrier-hosting potential compensation of electrodes, this work presents a valuable strategy towards achieving high-energy batteries, which could boost the development of other aqueous high-energy hybrid battery systems.

## Conflict of Interest

The authors declare no conflict of interest.

[1] a) Y. Zhang, H. Geng, W. Wei, J. Ma, L. Chen, C. C. Li, *Energy Storage Mater.* **2019**, *20*, 118-138; b) M. Mao, T. Gao, S. Hou, C. Wang, *Chem. Soc. Rev.* **2018**, *47*, 8804-8841; c) M. Rashad, M. Asif, Y. Wang, Z. He, I. Ahmed, *Energy Storage Mater.* **2020**, *25*, 342-375; d) G. Chen, Q. Huang, T. Wu, L. Lu, *Adv. Funct. Mater.*, *30, 2001289;* e) D. Bin, F. Wang, A. G. Tamirat, L. Suo, Y. Wang, C. Wang, Y. Xia, *Adv. Energy Mater.* **2018**, *8*, 1703008; f) D. Chao, W. Zhou, F. Xie, C. Ye, H. Li, M. Jaroniec, S.-Z. Qiao, *Sci. Adv.* **2020**, *6*, 4098; g) C. Han, J. Zhu, C. Zhi, H. Li, *J. Mater. Chem. A* **2020**, *8*, 15479-15512.

[2] a) F. Wang, X. Fan, T. Gao, W. Sun, Z. Ma, C. Yang, F. Han, K. Xu, C. Wang, *ACS Cent. Sci.* **2017**, *3*, 1121-1128; b) H. Zhang, D. Cao, X. Bai, *J. Power Sources* **2019**, *444*, 227-299.

[3] a) Y. Tang, X. Li, H. Lv, D. Xie, W. Wang, C. Zhi, H. Li, *Adv. Energy Mater.* **2020**, *10*, 2000892; b) L. Chen, J. L. Bao, X. Dong, D. G. Truhlar, Y. Wang, C. Wang, Y. Xia, *ACS Energy Lett.* **2017**, *2*, 1115-1121.

[4] a) M. Walter, K. V. Kravchyk, M. Ibáñez, M. V. Kovalenko, *Chem. Mater.* **2015**, *27*, 7452-7458; b) H. Dong, Y. Li, Y. Liang, G. Li, C.-J. Sun, Y. Ren, Y. Lu, Y. Yao, *Chem. Commun.* **2016**, *52*, 8263-8266.

[5] a) L. Chen, X. Fan, E. Hu, X. Ji, J. Chen, S. Hou, T. Deng, J. Li, D. Su, X. Yang, C. Wang, *Chem* **2019**, *5*, 896-912; b) Z. Liu, Y. Huang, Y. Huang, Q. Yang, X. Li, Z. Huang, C. Zhi, *Chem. Soc. Rev.* **2020**, *49*, 180-232.

[6] H. Li, L. Ma, C. Han, Z. Wang, Z. Liu, Z. Tang, C. Zhi, *Nano Energy* **2019**, *62*, 550-587.

[7] a) D. Xiao, Q. Dou, L. Zhang, Y. Ma, S. Shi, S. Lei, H. Yu, X. Yan, *Adv. Funct. Mater.* **2019**, *29*, 1904136; b) Q. Dou, Y. Lu, L. Su, X. Zhang, S. Lei, X. Bu, L. Liu, D. Xiao, J. Chen, S. Shi, X. Yan, *Energy Storage Mater.* **2019**, *23*, 603-609.

[8] a) J. Zhu, Y. Xu, Y. Fu, D. Xiao, Y. Li, L. Liu, Y. Wang, Q. Zhang, J. Li, X. Yan, *Small* **2020**, *16*, 1905838; b) F. Wang, O. Borodin, M. S. Ding, M. Gobet, J. Vatamanu, X. Fan, T. Gao, N. Eidson, Y. Liang, W. Sun, S. Greenbaum, K. Xu, C. Wang, *Joule* **2018**, *2*, 927-937; c) J. M. Wrogemann, S. Künne, A. Heckmann, I. A. Rodríguez-Pérez, V.

9

Siozios, B. Yan, J. Li, M. Winter, K. Beltrop, T. Placke, *Adv. Energy Mater.* **2020**, *10*, 1902709; d) X. Li, Y. Tang, J. Zhu, H. Lv, L. Zhao, W. Wang, C. Zhi, H. Li, *Small* **2020**, *16*, 2001935.

[9]   a) F. Wang, X. Fan, T. Gao, W. Sun, Z. Ma, C. Yang, F. Han, K. Xu, C. Wang, *ACS Cent. Sci.* **2017**, *3*, 1121-1128; b) D. Kundu, S. Hosseini Vajargah, L. Wan, B. Adams, D. Prendergast, L. F. Nazar, *Energy Environ. Sci.* **2018**, *11*, 881-892; c) Y. Xu, X. Deng, Q. Li, G. Zhang, F. Xiong, S. Tan, Q. Wei, J. Lu, J. Li, Q. An, L. Mai, *Chem* **2019**, *5*, 1194-1209; d) T. Liu, X. Cheng, H. Yu, H. Zhu, N. Peng, R. Zheng, J. Zhang, M. Shui, Y. Cui, J. Shu, *Energy Storage Mater.* **2019**, *18*, 68-91.

[10]  a) H. Zhang, K. Ye, K. Zhu, R. Cang, J. Yan, K. Cheng, G. Wang, D. Cao, *Chem. Eur. J.* **2017**, *23*, 17118-17126; b) H. D. Yoo, Y. Liang, H. Dong, J. Lin, H. Wang, Y. Liu, L. Ma, T. Wu, Y. Li, Q. Ru, Y. Jing, Q. An, W. Zhou, J. Guo, J. Lu, S. T. Pantelides, X. Qian, Y. Yao, *Nat. Commun.* **2017**, *8*, 339.

[11]  M. Liu, H. Ao, Y. Jin, Z. Hou, X. Zhang, Y. Zhu, Y. Qian, *Mater. Today Energy* **2020**, *17*, 100432.

[12]  a) H. Hu, Q. Li, L. Li, X. Teng, Z. Feng, Y. Zhang, M. Wu, J. Qiu, *Matter* **2020**, *3*, 95-126; b) Y. Dong, H. Shi, Z.-S. Wu, *Adv. Funct. Mater.*, **2020**, https://doi.org/10.1002/adfm.202000706; c) Q. Yang, Q. Li, Z. Liu, D. Wang, Y. Guo, X. Li, Y. Tang, H. Li, B. Dong, C. Zhi, *Adv. Mater.* **2020**, doi:10.1002/adma.202001854.

[13]  Y. Tang, Z. Zhao, X. Hao, Y. Wei, H. Zhang, Y. Dong, Y. Wang, X. Pan, Y. Hou, X. Wang, J. Qiu, *J. Mater. Chem. A* **2019**, *7*, 4469-4479.

[14]  X. Liu, Y. Cao, H. Zheng, X. Chen, C. Feng, *Appl. Surf. Sci.* **2017**, *394*, 183-189.

[15]  a) L. Shen, Y. Jiang, Y. Liu, J. Ma, T. Sun, N. Zhu, *Chem. Eng. J.* **2020**, *388*, 124228; b) S. Qiu, X. Wu, M. Wang, M. Lucero, Y. Wang, J. Wang, Z. Yang, W. Xu, Q. Wang, M. Gu, J. Wen, Y. Huang, Z. J. Xu, Z. Feng, *Nano Energy* **2019**, *64*, 103941; c) Z. Liu, G. Pang, S. Dong, Y. Zhang, C. Mi, X. Zhang, *Electrochim. Acta* **2019**, *311*, 1-7; d) X. Cao, L. Wang, J. Chen, J. Zheng, *J. Mater. Chem. A* **2018**, *6*, 15762-15770; e) Z. Guo, Y. Zhao, Y. Ding, X. Dong, L. Chen, J. Cao, C. Wang, Y. Xia, H. Peng, Y. Wang, *Chem* **2017**, *3*, 348-362; f) Q. Li, N. Li, Y. Liu, Y. Wang, H. Zhou, *Adv. Energy Mater.* **2016**, *6*, 1600632.

[16]  a) Y. Yuan, D. Bin, X. Dong, Y. Wang, C. Wang, Y. Xia, *ACS Sustain. Chem. Eng.* **2020**, *8*, 3655-3663; b) M. Shao, J. Deng, F. Zhong, Y. Cao, X. Ai, J. Qian, H. Yang, *Energy Storage Mater.* **2019**, *18*, 92-99; c) H. Zhang, K. Ye, K. Zhu, R. Cang, J. Yan, K. Cheng, G. Wang, D. Cao, *Electrochim. Acta* **2017**, *256*, 357-364; d) X. Dong, L. Chen, X. Su, Y. Wang, Y. Xia, *Angew. Chem. Int. Ed.* **2016**, *55*, 7474-7477; e) Z. Li, D. Young, K. Xiang, W. C. Carter, Y.-M. Chiang, *Adv. Energy Mater.* **2013**, *3*, 290-294.

[17]  H.-S. Kim, J. B. Cook, H. Lin, Jesse S. Ko, Sarah H. Tolbert, V. Ozolins, B. Dunn, *Nat. Mater.* **2017**, *16*, 454-460.

[18]  D. Chao, C. Zhu, P. Yang, X. Xia, J. Liu, J. Wang, X. Fan, S. V. Savilov, J. Lin, H. J. Fan, Z. X. Shen, *Nat. Commun.* **2016**, *7*, 12122.

[19]  a) G. Fang, Z. Wu, J. Zhou, C. Zhu, X. Cao, T. Lin, Y. Chen, C. Wang, A. Pan, S. Liang, *Adv. Energy Mater.* **2018**, *8*, 1703155; b) Y. You, H.-R. Yao, S. Xin, Y.-X. Yin, T.-T. Zuo, C.-P. Yang, Y.-G. Guo, Y. Cui, L.-J. Wan, J. B. Goodenough, *Adv. Mater.* **2016**, *28*, 7243-7248.

[20]  Y. Tang, Z. Zhao, Y. Wang, Y. Dong, Y. Liu, X. Wang, J. Qiu, *ACS Appl. Mater. Inter.* **2016**, *8*, 32324-32332.

[21]  D. Kundu, B. D. Adams, V. Duffort, S. H. Vajargah, L. F. Nazar, *Nat. Energy* **2016**, *1*, 16119.

[22]  F. Mo, G. Liang, Q. Meng, Z. Liu, H. Li, J. Fan, C. Zhi, *Energy Environ. Sci.* **2019**, *12*, 706-715.

10

## Entry for the Table of Contents
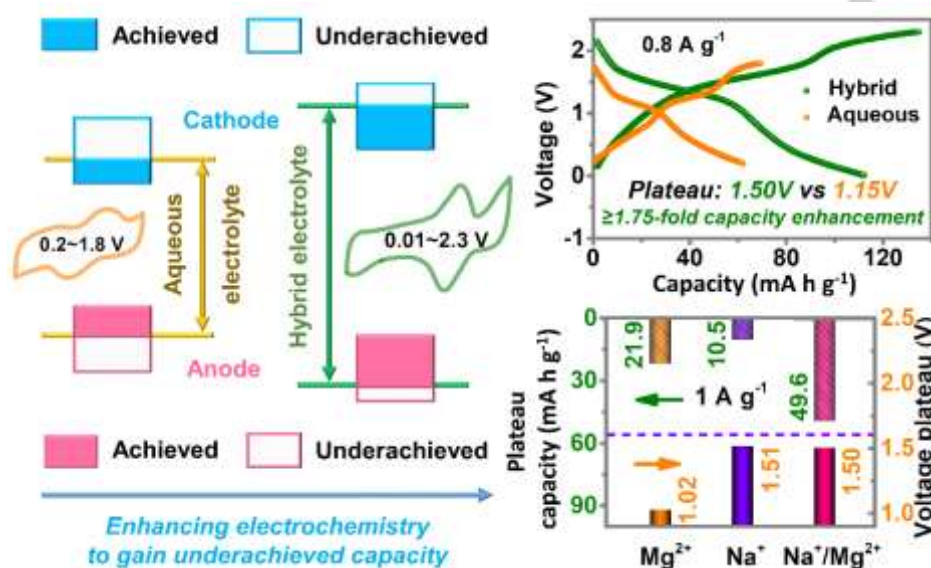


High-energy magnesium hybrid full batteries were built by initially coupling $Mg_{1.5}VCr(PO_4)_3$ cathode with $FeVO_4$ anode in aqueous/organic $Mg^{2+}/Na^+$ hybrid electrolyte. Benefiting from enhanced electrochemistry with carrier-hosting potential compensation, the batteries delivered a high voltage plateau of ~1.50 V and a capacity (233.4 mA h g$^{-1}$ at 0.5 A g$^{-1}$, 92.7 Wh kg$^{-1}$electrode) that is ≥1.75-fold higher than those achieved in conventional aqueous electrolytes.